Plasma Sources Science and Technology

PAPER

Hall thruster operation with externally driven breathing mode oscillations

IOP Publishing Plasma Sources Science and Technology
Plasma Sources Sci. Technol. 27 (2018) 094006 (12pp) https://doi.org/10.1088/1361-6595/aadf06

Hall thruster operation with externally driven breathing mode oscillations

I Romadanov[1,2], Y Raitses[1] and A Smolyakov[2]

[1] Princeton Plasma Physics Laboratory, Princeton, NJ 08543, United States of America
[2] University of Saskatchewan, Saskatoon, SK S7N5E2, Canada

E-mail: ivr509@mail.usask.ca

Received 12 July 2018, revised 21 August 2018
Accepted for publication 5 September 2018
Published 25 September 2018

Abstract

The discharge and plasma plume characteristics of the cylindrical Hall thruster were studied in regimes with external modulations of the applied voltage. It is found that the amplitude and the root mean square (rms) value of the discharge and ion currents increase with the amplitude of the external modulation exhibiting two different regimes. For smaller amplitudes of the modulation voltage, the oscillations amplitude and rms value of the discharge and ion currents follow the amplitude of modulations approximately linearly. For larger voltage modulations, the amplitude and the rms value of the discharge and ion currents grow faster and nonlinearly. In the nonlinear regime, the discharge and the ion currents demonstrate pronounced dependence on the frequency of the external modulations. Moreover, the rms value of the ion current is amplified stronger than the rms value of the discharge current resulting in an increase of the current utilization (of about 5%) and the propellant utilization efficiencies (of about 40%). The thruster efficiency, defined as a product of the current and propellant utilization coefficients, shows an increase of the about 20%. We also present the results of theoretical modeling of a plasma response to driven oscillations in a simplified 1D model of resistive-ionization mode in quasineutral plasma. This modeling demonstrates the nonlinear property of the fundamental breathing mode similar to the experimental results.

Keywords: plasma propulsion, Hall thruster, efficiency, breathing mode, oscillations control, modeling

1. Introduction

Hall thrusters are satellite propulsion devices, which accelerate the plasma in applied crossed electric and magnetic fields. The description of the design, and operation characteristics can be found elsewhere (see, for example [1–3]. A typical Hall thruster is powered by a DC power supply operating in voltage regulated mode. Since the voltage is kept constant, the thruster exhaust velocity, V_{ex}, or specific impulse $I_{sp} = V_{ex}/g$, where g is the gravity is assumed to be constant as well. Despite DC input power, Hall thruster operation is often a subject to low-frequency oscillations [4] of the discharge current or so-called breathing oscillations, which have characteristic frequency about 10–20 kHz [5, 6]. These oscillations can be very powerful with almost 100% of the steady-state values of discharge current and are usually non-stationary and semi-coherent in time. Such strong oscillations may result in unstable thruster operation and cause degradation of the thruster performance, and the reduction of the thruster lifetime [7–10]. The physical mechanism responsible for breathing oscillations is usually attributed to some sort of ionization instability [11–13].

Since the introduction of the Hall thruster concept in late 60s of the last century, many studies and developments were focused on understanding and mitigation of breathing oscillations. In the present work, we explore an approach to control breathing oscillations by modulating the applied voltage. In our recent studies, we already demonstrated this approach with application to time-resolved laser-induced fluorescence diagnostic [14]. The applied voltage was externally modulated by adding a sinusoidal voltage component to the anode potential. These studies revealed a nonlinear response of the ion velocity distribution function (IVDF) to the voltage modulations. In this work, we study the effect of

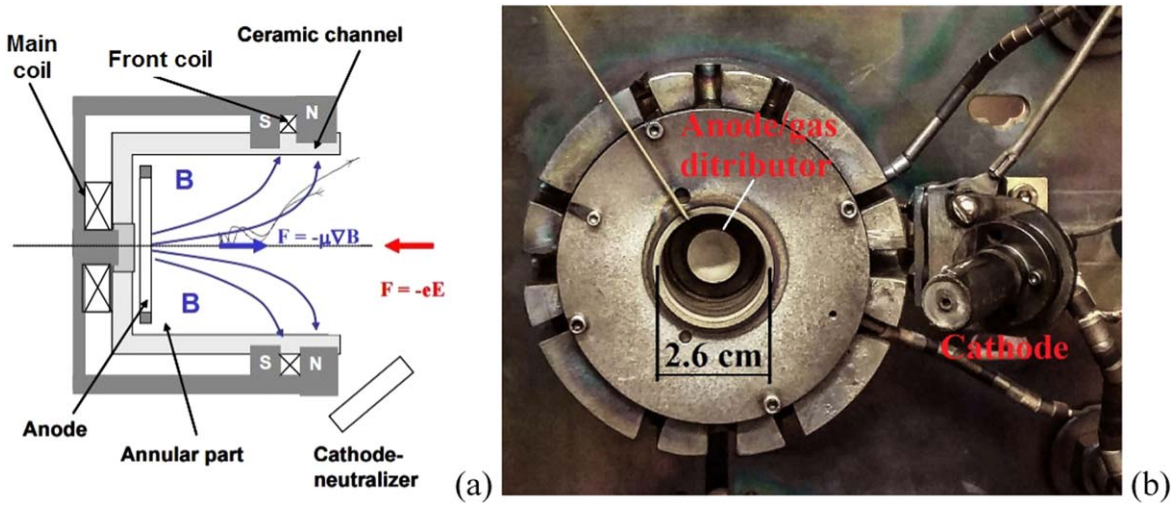

Figure 1. (a) CHT schematic; (b) 2.6 cm CHT.

voltage modulations, including their amplitude and frequency, on the discharge and the ion currents, and its implications on the thruster performance. Because of the increase in the discharge current and faster growth of the ion current, compared to the discharge current, increase in the thruster efficiency, in terms of the propellant utilization and current utilization, was expected.

2. Experimental setup

For studies of breathing oscillations, we use the cylindrical Hall thruster (CHT). Similar to conventional annular design Hall thrusters (so-called stationary plasma thruster or SPT), the CHT accelerates the ions by $E \times B$ fields [15]. The main difference from SPT thrusters is that CHT has a cylindrical channel with diverged magnetic fields. In present research a 200 W CHT with 2.6 cm channel diameter was used (see figure 1) [16].

This CHT has two electromagnet coils—back coil and front coil [17] which are used to produce and control the magnetic field distribution in the CHT channel. The description of this thruster design and operation can be found in [16–19]. The thruster was powered by a DC power supply and operated at the discharge (anode) voltage of 220 V. This voltage was chosen because the natural breathing mode exists at this operation condition. Xenon gas was used as a propellant with 3.5 sccm flow rate through the anode and 2 sccm though the cathode-neutralizer. In the described experiments, currents in both electromagnetic coils were co-directed to form the so-called direct magnetic configuration with diverging magnetic field [18]. Experiments were conducted in the small Hall thruster facility at PPPL [19] equipped with a turbo-molecular pumping system. During the thruster operation, the background pressure did not exceed 70 μTorr.

To study the breathing oscillations and their control, the electrical circuit of the thruster discharge was modified compared to previous experiment [20], so the modulations can be added to the applied DC discharge voltage (see figure 2). In particular, amplitudes and frequencies of the modulation voltage were controlled with a function generator. Its signal was amplified and then added to the DC level of the anode potential by Kepco BOP50-4M amplifier, which was connected in series with the thruster power supply. The amplitude of the modulation V_{mod} was varied from 8 to 50 V peak-to-peak. The upper limit was determined by the thruster stable operation. The modulation frequency was varied from 6 to 18 kHz.

Two main parameters were measured during these experiments: the discharge current (I_d) and the ion (or beam) current (I_b). The discharge current was measured using a low impedance current shunt placed in the thruster electrical circuit between the thruster and the modulation amplifier [21]. Measurements of the ion current were done with a negatively biased (to −40 V) movable flat electrostatic graphite probe with a guarding sleeve [22]. Probe was located on the rotating arm and distance from the CHT exit plane to the collecting surface of the probe was 14 cm. The total ion flux was determined by integrating over the measured angular ion flux distribution [17, 23]. Detailed description of the procedure is given in appendix A. Schematics of the planar probe measurements and general experiment scheme are shown in figure 3. In addition, in a separate set of experiments, the IVDF was measured using laser induced florescence diagnostic. Moreover, the plasma properties at the channel exit of the CHT, including plasma potential, plasma density and the electron temperature were measured too. Results of these probe and IVDF measurements are described in [24].

As is described in the appendix B, we have investigated the circuitry response to modulations without the thruster to ensure that the observed phenomena do not come from the power supply.

3. Experimental results and discussions

The linear and nonlinear responses of the thruster to the anode potential modulation were described in [14]. The linear

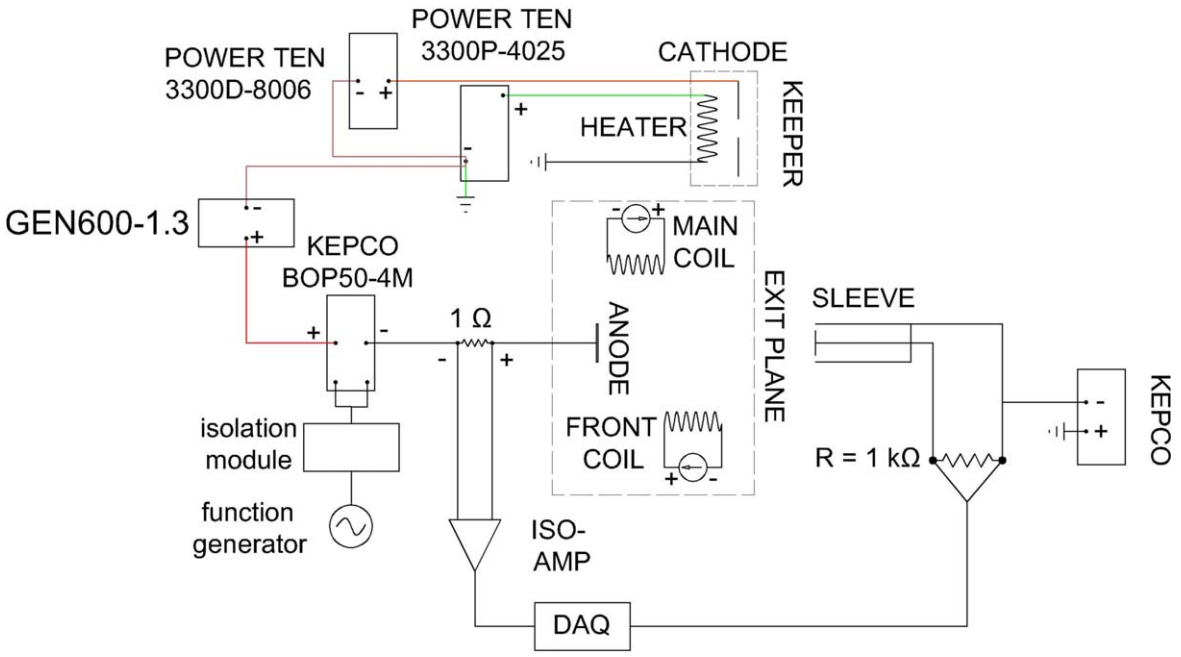

Figure 2. Electric schematic for the driving circuit and the planar probe measurements.

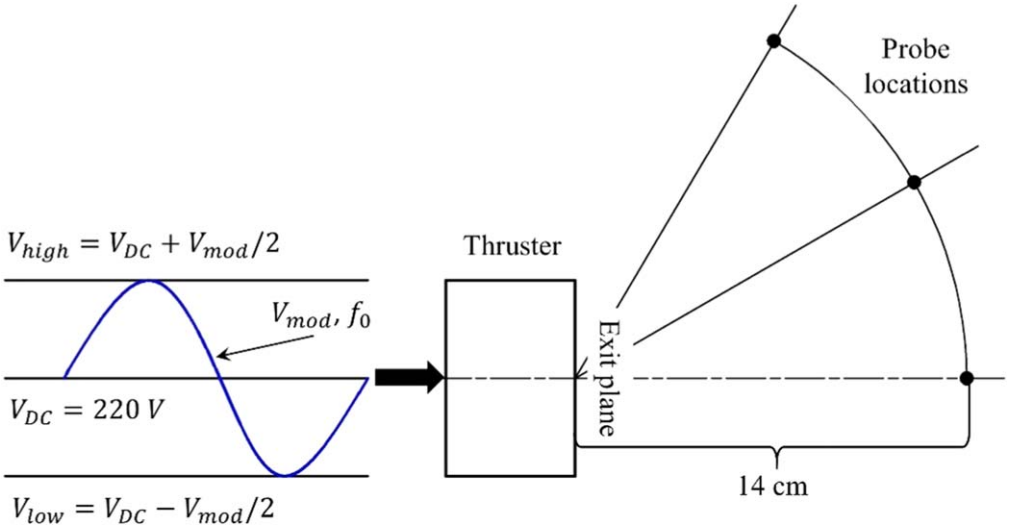

Figure 3. Schematics of the anode potential modulation and the planar probe measurements, where V_{DC} is the anode applied voltage, V_{mod} is the modulation voltage with the frequency f_0.

response was identified as a regime when the amplitude of the discharge current grows linearly with the increase in the modulation voltage amplitude, while the rms value remains approximately constant. The nonlinear response was defined as the thruster regime when modulation of the discharge voltage results in stronger (faster) increase of the rms of the discharge current. In this regime, there is a nonlinear rise in the root mean square (rms) value and oscillation amplitudes (figure 4).

3.1. Effect of the modulation amplitude and frequency on the discharge current and ion current oscillations

Without the applied modulation, the discharge current exhibits intrinsic breathing oscillations at a frequency about 13 kHz. With the applied modulations, the amplitude of the current oscillations depends on the modulation amplitude. This dependence has a resonant-kind behavior reaching maximum amplitude at a certain modulation frequency. We define the resonant modulation frequency as the frequency at which rms value of the current oscillations and their amplitude reached maximum. In the described experiments, this frequency was determined by monitoring the discharge current oscillation amplitude while modulation frequency was varied (figure 5). When the modulation amplitude was below 10% of the DC discharge voltage level, the resonance was at frequency near the frequency of natural breathing oscillations ~12–13 kHz. This can be seen in figure 5(a), at the modulation amplitude of $V_{mod} = 16$ V the rms value and

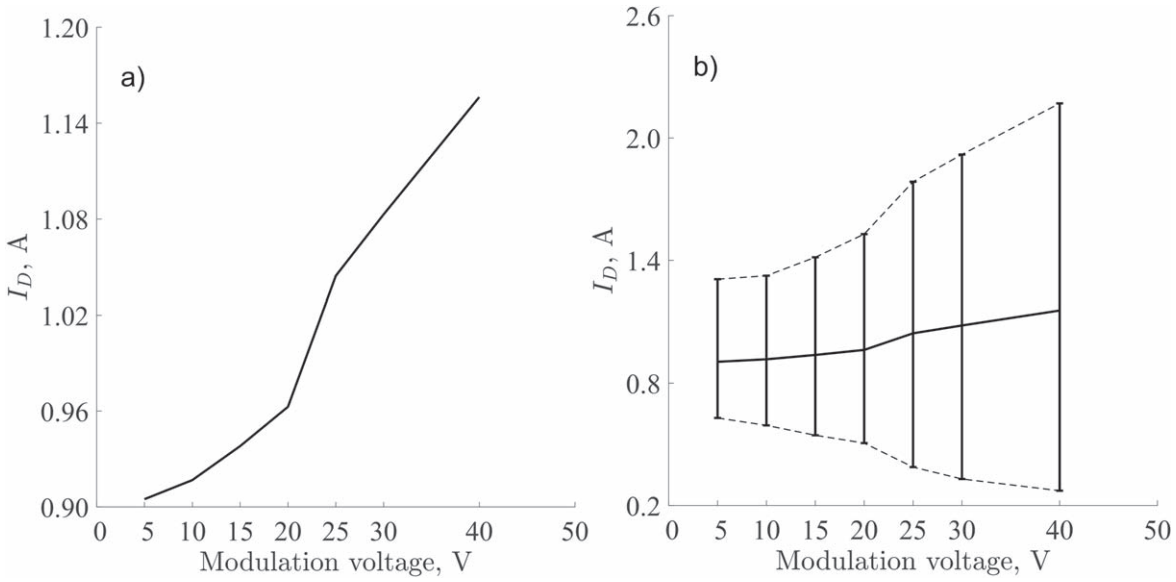

Figure 4. (a) Rms value of the discharge current as a function of the external modulation voltage. (b) Amplitudes of the discharge current oscillations as a function of the external modulation voltage. Dashed lines represent maximums and minimums of the oscillations amplitude.

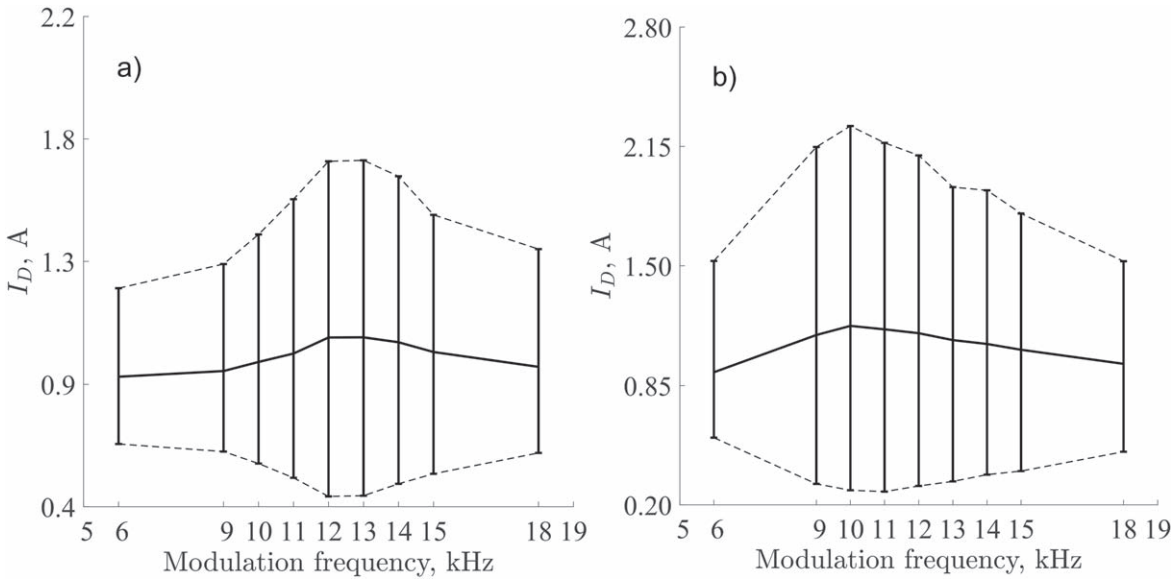

Figure 5. Rms values of the discharge current as a function of the external modulation frequency at (a) $V_{\mathrm{mod}} = 16$ V; (b) at $V_{\mathrm{mod}} = 40$ V. Dashed lines represent maximums and minimums of oscillation amplitude.

corresponding amplitude (shown with vertical bars) of the discharge current reach their maximum at ∼13 kHz of the modulation frequency. At higher values of the modulation amplitude, the resonance frequency shifts towards the lower frequencies ∼10 kHz. In figure 5(b), when $V_{\mathrm{mod}} = 40$ V, the maximum of the rms value and the oscillation amplitude is at ∼10 kHz.

Therefore, the increase of the modulation amplitude leads not only to the nonlinear increase of the rms value of the discharge current but affects the resonance frequency as well. To investigate this behavior, the anode potential of the thruster was modulated with frequencies in the range from 6 to 18 kHz, and amplitudes in the range from 5 to 50 V peak-to-peak. The discharge and the ion currents were monitored; results are shown in figure 6. At $V_{\mathrm{mod}} = 50$ V and modulation frequencies below 13 kHz, thruster operated very unstable and it was impossible to collect data.

As it shown in figure 6, there is a growth of the rms values of the discharge current and the ion current with the increase of the modulation amplitude. At low amplitudes, rms values are not affected by frequency change. However, with the increase of the modulation amplitude, there is a clear resonant behavior with a maximal response at a frequency which shifts towards lower values for higher modulation amplitude.

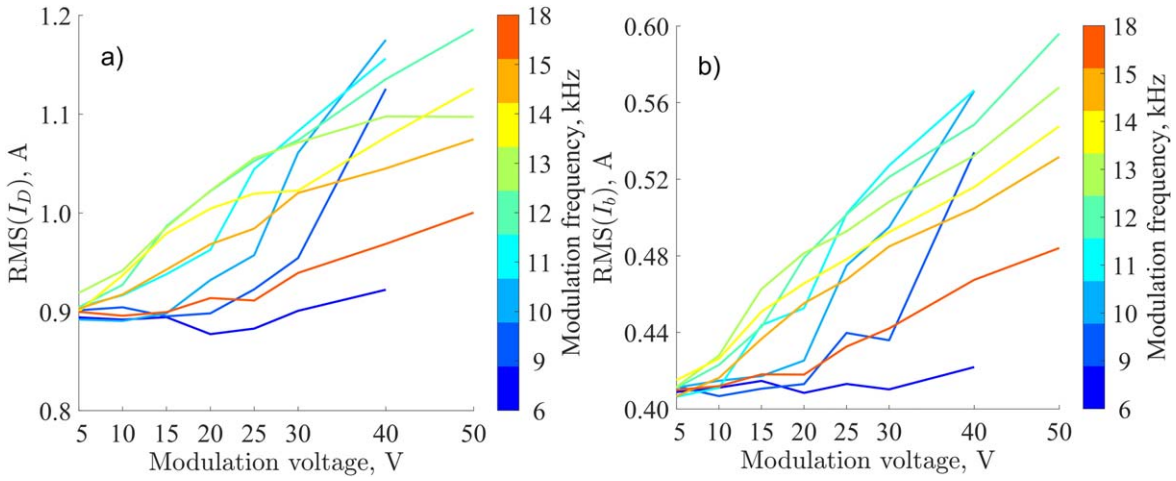

Figure 6. Rms value of the discharge current (a) and the ion current (b) as a function of the amplitude of the external modulation and at different modulation frequencies. Different colors on the color bar represent different modulation frequencies.

3.2. Effect of the modulation on the thruster efficiency

The thruster efficiency is the ratio of the thruster kinetic power to the input electric power. It can be characterized in terms of the current utilization, the propellant utilization, and the voltage utilization [2, 15]. The total thruster efficiency is defined as

$$\eta_T = \frac{T^2}{2\dot{m}_p P_{\text{in}}} = \gamma^2 \eta_b \eta_v \eta_m \eta_0, \tag{1}$$

where T is the thrust, $\dot{m}_p$ is the total propellant mass flow, γ is the beam divergence, η_b is the current utilization, η_v is the beam voltage utilization, η_m is the propellant utilization, and η_0 is the electrical utilization efficiency. In this work we investigate only effects from the current utilization and the propellant utilization.

The current utilization is defined as

$$\eta_b = \frac{I_b}{I_d}, \tag{2}$$

where I_b is ion beam current, I_d is the total discharge current. It shows what part of the discharge current goes to the ion current, and it is limited by the axial electron current, because $I_d = I_e + I_i$.The propellant utilization is defined as

$$\eta_m = \frac{\dot{m}_i}{\dot{m}_a} = \frac{I_i}{I_m}, \tag{3}$$

where $\dot{m}_i$ is the ion mass flow, $\dot{m}_a$ is the anode flow rate, and $I_i = e\dot{m}_i/M_i$ and $I_m = e\dot{m}_a/M_i$, here e is the charge and M_i is the xenon atom mass. We did not account for the cathode flow rate. This coefficient reflects the efficiency of the ion production, affected by the losses in the channel.

Results for the current utilization are shown in figure 7. In the linear regime, when the modulation amplitude is small, the current utilization remains approximately constant at all frequencies. In the nonlinear regime when modulation amplitude increases, the current efficiency slightly increases, but there is not clear dependency on the modulation frequency.

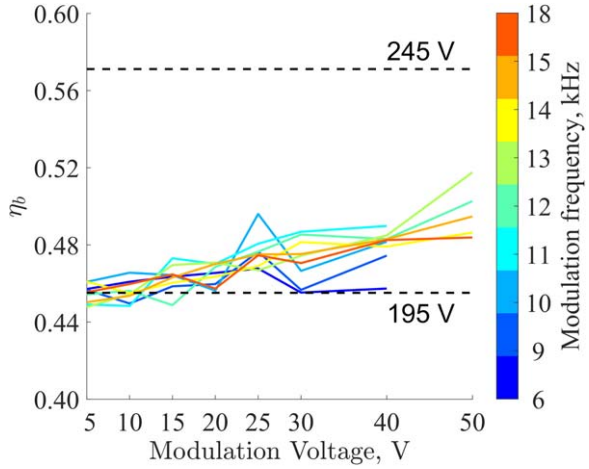

Figure 7. The current utilization as a function of the amplitude of the external modulation and at different modulation frequencies. Different colors on color bar represent different modulation frequencies. Dashed lines show current utilization at 195 and 245 V discharge voltage without any modulation.

Figure 8 shows that the propellant utilization increases significantly with the increases of the modulation amplitude. This increase reaches its maximum at the resonant frequency, which depends on the amplitude as well.

Propellant and current utilization efficiencies were deduced from measured results for the discharge voltages of 195 and 245 V DC without the external modulation for the comparison. These values correspond to maximum and minimum levels of the discharge voltage during the modulation around 220 with 50 V amplitude. As it is shown in figures 7 and 8, there is a strong evidence of the increased ionization during the modulation. The propellant utilization growth is significant even in comparison with the 245 V level.

Finally, the total contribution to the thruster efficiency was estimated as a product of the propellant the current utilization efficiencies. Results are shown in figure 9. It can be seen, that when modulation is at resonant frequency and amplitude is large, efficiency can be increased up to 20%.

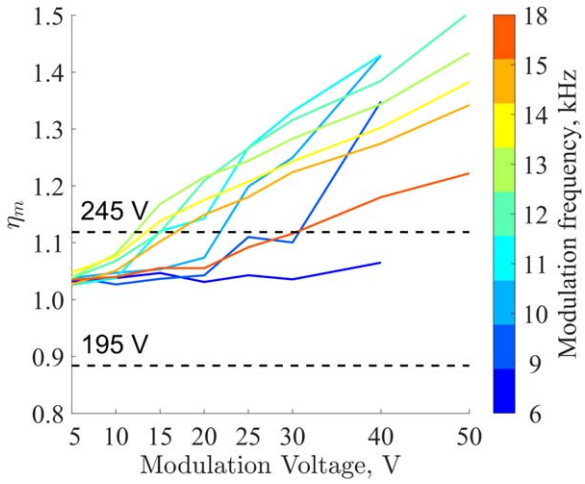

Figure 8. The propellant utilization as a function of the amplitude of the external modulation and at different modulation frequencies. Different colors on color bar represent different modulation frequencies. Dashed lines show current utilization at 195 and 245 V discharge voltage without any modulation.

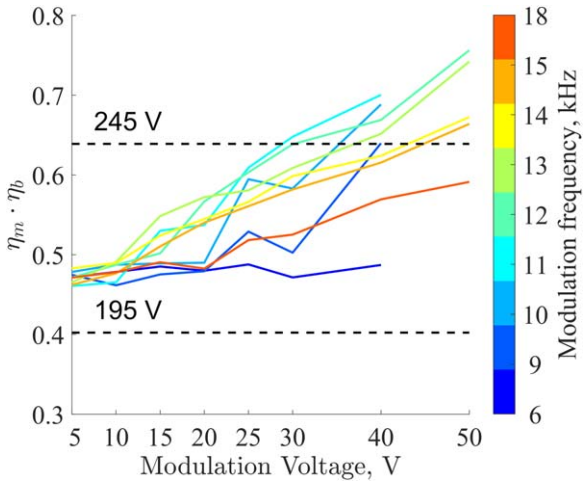

Figure 9. Product of the propellant utilization and the current utilization as a function the amplitude of the external modulation and at different modulation frequencies. Different colors on color bar represent different modulation frequencies. Dashed lines show current utilization at 195 and 245 V discharge voltage without any modulation.

However, in comparison with the 245 V DC discharge without the external modulation, increase is only about 10%.

It is important to notice, that beam divergence is almost unaffected by the external modulations. Results of measurements of ion beam divergence are presented in appendix A, figure A1. As one can see, divergence is almost the same as in case of the linear regime (figure A1(a)) and in case of the nonlinear regime (figure A1(b)). Therefore, beam divergence coefficient γ remains approximately unchanged.

4. Theoretical modeling of externally driven ionization breathing mode

In this section, we consider a simple time dependent 1D model of ion acceleration across the magnetic field in a quasineutral plasma. This is the simplest model used to describe the stationary flows of ions [25–28] as well as breathing modes oscillations in Hall thrusters. It is a time dependent, 1D with model with three species: neutrals, singly charged ions, and electrons. Neutrals are injected with constant velocity $v_a = \text{const}$ at the left side of the simulation region and described by continuity equation

$$\frac{\partial n_a}{\partial t} + v_a \frac{\partial n_a}{\partial x} = -\beta n_a n_i. \tag{4}$$

The neutral flow is depleted due to ionization with a constant ionization rate β. Respectively, the ion and electron continuity equations have the source due to ionization on the right-hand side

$$\frac{\partial n_i}{\partial t} + \frac{\partial n_i v_i}{\partial x} = \beta n_a n_i, \tag{5a}$$

$$\frac{\partial n_e}{\partial t} + \frac{\partial n_e v_e}{\partial x} = \beta n_a n_e. \tag{5b}$$

Ionization adds the drag to the ion acceleration (given by the last term) in the ion momentum balance

$$\frac{\partial v_i}{\partial t} + v_i \frac{\partial v_i}{\partial x} = \frac{e}{m_i} E + \beta n_a (v_a - v_i), \tag{6}$$

here β is the ionization rate, v_a is the neutral flow velocity, and v_i is the ion flow velocity. The electrons are modeled in the drift-diffusion approximation

$$0 = e n_e \mu_e E - e \mu_e \frac{\partial T_e n_e}{\partial x} - m_e n_e \nu_e, \tag{7}$$

where μ_e is the electron mobility perpendicular magnetic field, v_e is the electron flow velocity, T_e is the electron temperature. The diffusion (due to pressure gradient) is especially important near the anode, or in the so-called diffusion region, resulting in the inversion of the electric field in this region and leading to a backflow of ions to the anode. Our model is quasineutral, so there is no sheath effect included. By using the quasineutrality $n_i = n_e = n$ condition equations (5*a*), (5*b*) become

$$\frac{\partial}{\partial x}(n_e v_e + n_i v_i) = 0.$$

Then the Ohm's law can be written as

$$E = \frac{J_d}{e n \mu_e} - \frac{v_i}{\mu_e} - \frac{1}{en} \frac{\partial (T_e n)}{\partial x}, \tag{8}$$

where $J_d = e(n_i v_i - n_e v_e)$ is the total current density which is uniform in space but can oscillate in time. The electric field in the system is constrained by the potential drop U_d between anode and cathode

$$\int_0^L E \mathrm{d}x = U_d,$$

where L is the channel length (neglecting the sheath voltage).

The external voltage U_d will be modulated in time. The electron mobility μ_e is given by the classical expression for collisional transport in the transverse magnetic field is:

$$\mu_e = \frac{e}{m_e \nu_m} \frac{1}{1 + \omega_{ce}^2 / {\nu_m}^2},$$

where $\omega_{ce} = eB/m_e$ is the electron cyclotron frequency, and ν_m is the total electron momentum exchange collision frequency. Note that in thruster conditions the value of μ_e is likely to be anomalous so the electron transport model should be viewed as a simple parametrization of anomalous mobility and diffusion rather than exact equation based on the classical transport coefficients.

This model neglects a number of effects, e.g. sheath wall losses and wall recombination effects due to 2D geometry. Several other simplifications are invoked such as constant electron temperature (and, therefore, the ionization coefficient), electron mobility (and Hall parameter), and neutral velocities.

As such, our model does not reproduce exact experimental conditions. Neither the anomalous conductivity is well known for these conditions. Therefore, here we do not attempt to match the outcome of our theoretical model with experimental data. Our goal is to demonstrate that the basic model of ionization modes in $E \times B$ discharge as given above (and as was used in [25, 26]) is capable of capturing the nonlinear phenomena which occurs during the external modulations of the applied voltage.

The ion acceleration within the framework of equations (5)–(6) exhibits a removable singularity at the sonic point where the ion velocity is equal to the ion sound velocity [26, 27]. The conditions that the sonic point becomes regular impose strong constraints on the stationary solutions as has been recently discussed in [29].

The full system of nonlinear equations (4)–(8) was solved in BOUT++ framework [30–32] as an initial value problem. Upwind terms in these equations were treated with third order central WENO scheme. This scheme allows to simulate flows from subsonic to supersonic and deals with shock wave discontinuities.

4.1. Simulation parameters

Simulations were conducted with parameters close to ones measured during the CHT operation. List of typical values is shown in table 1.

It is important to notice, that the initial value simulations in this model require boundary conditions (B.C.) at the anode [29]. These B.C. were defined from stationary solutions of the above system of equations obtained by different method [26, 27].

4.2. Intrinsic breathing mode oscillations

First, the natural (intrinsic) breathing oscillations were obtained for the given set of parameters and in neglect of the external modulations. Initial value simulations were started with arbitrary profiles for n_i, n_a, and v_i, and B.C. defined from stationary solutions. The system shows intrinsic breathing mode oscillations as shown in figure 10. Rms value of the discharge current I_d is equal to the value obtained from the stationary solution. There are current oscillations with the frequency $f_0 = 79.1$ kHz, and amplitude about 0.4 A peak-to-peak. It is important to note that the self-consistent dynamics of the electric field, ion and electron response, together with ionization is important for the occurrence of oscillations [33]. No oscillations can be obtained with continuous analog of the predator–prey model; i.e. exclusively within the coupled ion-neutral dynamics [34] alone and neglecting the electrons and total current coupling. Also note that since our model assumes the constant electron temperature, the feedback coupling mechanism for the oscillations discussed in [13, 35] is not involved.

The intrinsic oscillations in our model have the frequency different from the one observed in experiments. It was shown previously that the oscillation frequency is very sensitive to the value of the mobility [33]. Inhomogeneous magnetic field (inhomogeneous mobility) also affects the frequency of oscillations. The constant value of Hall parameter $\beta = 0.11$ was used in our simulations. Since the value of the anomalous mobility was not well known in our experiments, we did not attempt to match the frequency to experimental value by varying the anomalous mobility and other plasma parameters. However, nature of those oscillations is the same as for oscillations in [11, 36, 37].

Table 1. Simulation parameters.

Parameter	Value
Gas	Xenon
Channel length, L	3.0 cm
Channel radius, r	1.2 cm
Channel area, A	4.5 cm^2
Mass flow, $\dot{m}$	0.34 mg s^{-1}
Discharge current, I_d	0.8 A
Discharge voltage, U_d	230.8 V
Electron temperature, T_e	20 eV
Ion sound, c_s	3833 m s^{-1}
Neutral velocity, v_a	200 m s^{-1} ($T_a \approx 650$ K)
Collision frequency, ν_m	10^6 s^{-1}
Electron mobility, μ_e	0.1, m^2 V^{-1} s^{-1}

4.3. Effect of the discharge voltage modulations

The discharge voltage was modulated by applying a sin wave at a frequency equal to the intrinsic breathing oscillations frequency $f_0 = 79.1$ kHz. Modulation amplitudes V_{mod} were chosen to be in the range 5%, 12.5%, 25%, and 50% of the applied potential U_d. The resulting rms values of the discharge and ion currents, and their oscillation amplitudes as a function of the modulation amplitude are shown in figure 11.

Similar to the experiments, we observe a nonlinear increase of the discharge current rms value and oscillation amplitude with the modulation amplitude (see figures 4 and 5). Same behavior is observed for the ion current.

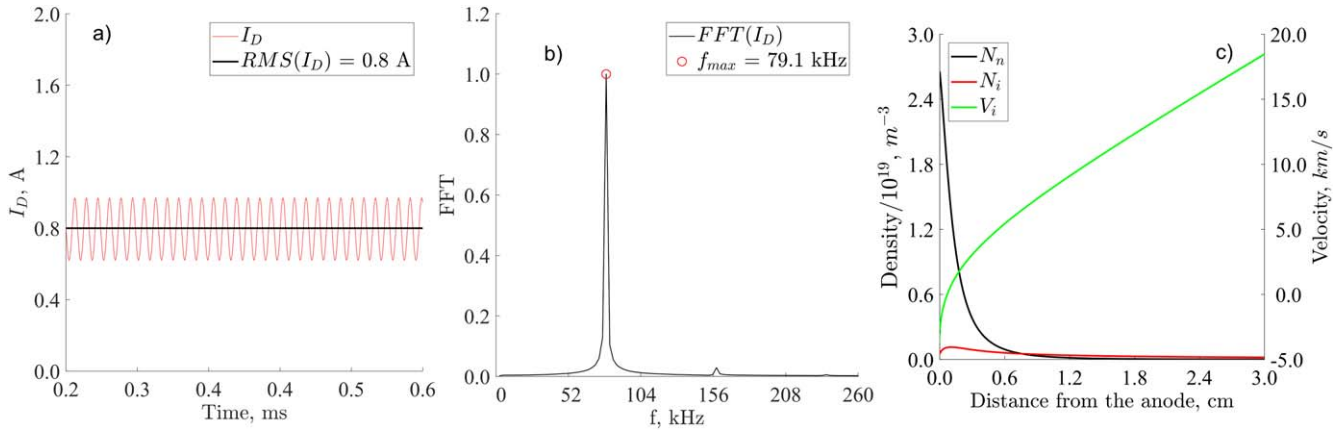

Figure 10. (a) The discharge current I_d trace. (b) Fast Fourier transform of I_d. (c) Averaged in time profiles of n_i (red), n_a (black), and v_i (green).

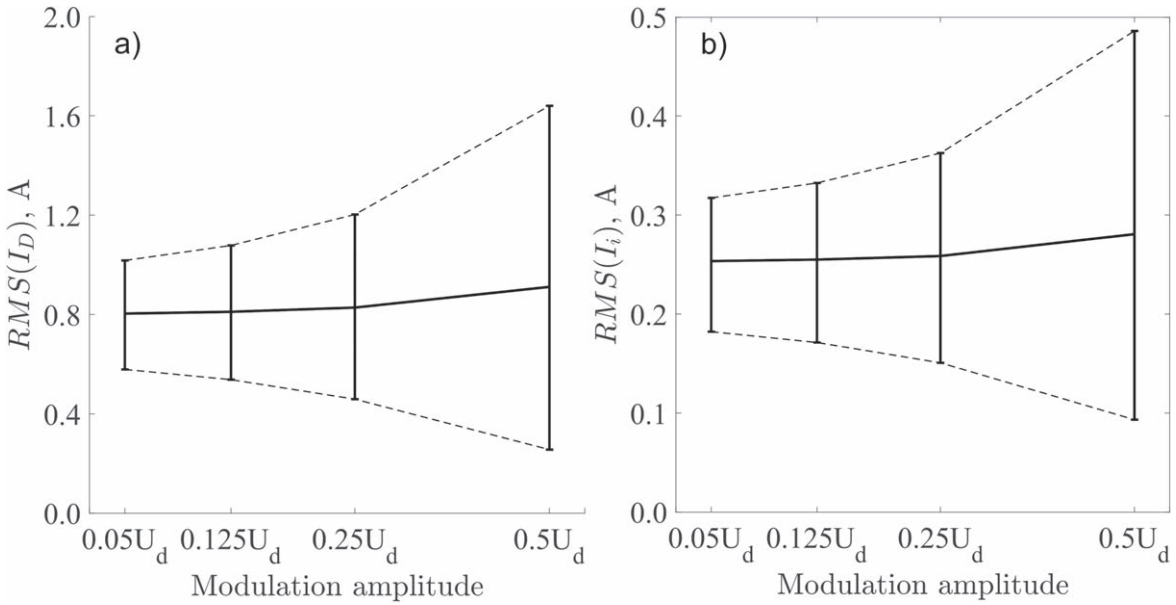

Figure 11. The rms values of (a) the discharge current I_d; (b) the ion current I_i, and corresponding oscillation amplitudes as a function of modulation voltage.

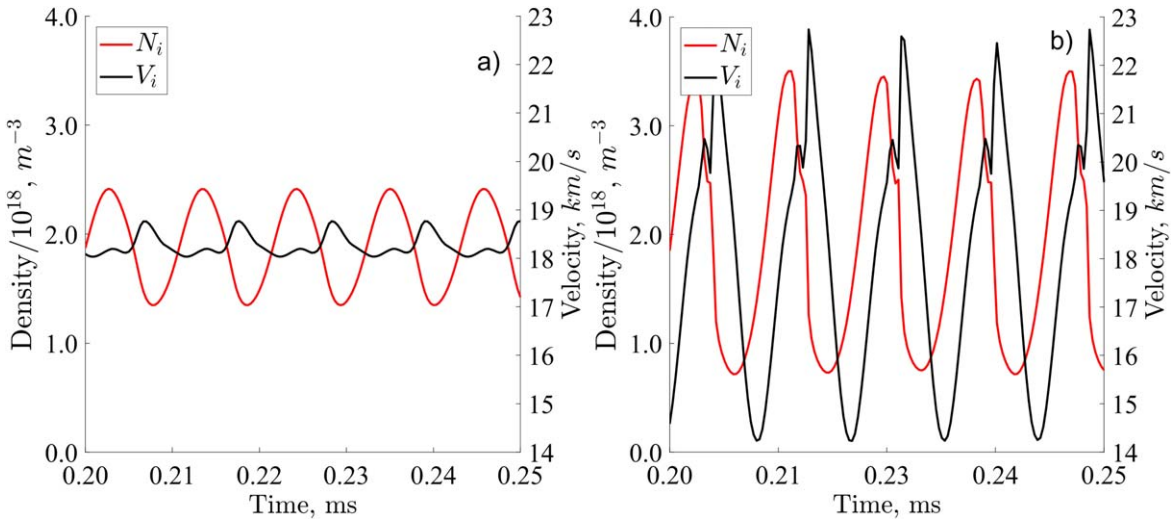

Figure 12. Ion density and ion velocity at the exit plane at (a) $V_{\text{mod}} = 0.05U_d$, and (b) $V_{\text{mod}} = 0.5U_d$ modulation amplitude.

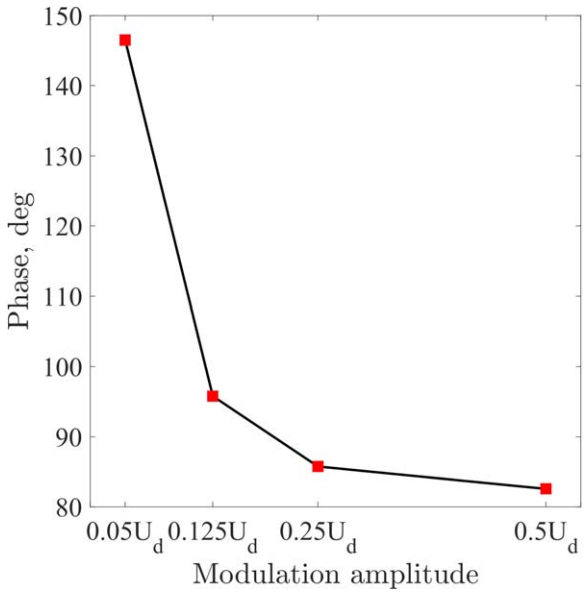

Figure 13. Phase difference between ion velocity and ion density as a function of modulation amplitude in the simulation.

We have studied the behavior of the ion velocity v_i and ion density n_i at the channel exit. Examples of such time traces for $V_{\mathrm{mod}} = 0.05U_d$—linear regime and $V_{\mathrm{mod}} = 0.5U_d$—nonlinear regime are shown in figures 12(a), (b) respectively.

There is a noticeable difference between the linear and nonlinear regimes. First, one observes an increase in the amplitude of oscillation for larger modulation amplitude. One can also see that in nonlinear regime the modulated v_i acquires the higher nonlinear harmonics (second and higher). The contribution of the quadratic terms (e.g. $\sin^2$) to the mean values is in part responsible for the rms enhancement. Secondly, there is a strong reduction of the phase difference between density and ion velocity oscillations with increase of modulation as shown in figure 13, so that the enhanced correlation result in the increase of the mean value.

This reduction of phase differences was confirmed by experimental measurements in the linear and nonlinear regimes, [24]. Measurements were done for two modulation amplitudes: 16 V_{pp} and 32 V_{pp}. The procedure for probe data processing can be found, for example, in [38]. Phase differences between the ion density, the acceleration potential, the modulation voltage and the discharge current signal were obtained. Phasor plot is a simple way to show phases between different signal. Phasor is a vector, with length equal to the amplitude of the signal and directed at angle, which represents a phase shift.

Each signal has its amplitude and phase shift with respect to some base signal. The modulation voltage signal was chosen as a base signal. Phase difference between signals was determined by applying Hilbert transform to each signal, and then calculating corresponding angle between transformations. The more detailed description can be found in [39]. After these procedure phases ϕ were obtained for each signal. Time lag due to different probe position was included as well. Amplitude of signals is not important in this analysis, so amplitude of each signal was set to unity. Two phasor plots, for linear and nonlinear regimes are show in figures 14(a) and (b) respectively. The modulation voltage signal (red) was chosen to be the reference once, and it has 0 phase shift. The discharge current (orange) and the ion density (green) oscillations coincide for the linear regime and are almost in phase for the nonlinear regime. The acceleration potential (yellow) was measured during the experiment, and the electric field was obtain by shifting it by $\pi/2$. As one can see, there is a reduction in phase between the electric field and the ion density.

Similar behavior for the electric field is observed for our simulations. The ion density and the electric field trace for linear and nonlinear regimes are shown in figures 15(a) and (b) respectively. Phase shift reduced significantly for the nonlinear regime.

Therefore, the observed increase of the ion current is related to the increase of the amplitude of oscillations as well as to the reduction of phase shift between density and electric field (or ion velocity) oscillations.

5. Conclusions

In this paper, we report on the studies of the thruster response to the externally applied modulations of the DC discharge voltage. Application of external modulations in the frequency range of breathing oscillations (6–18 kHz) results in increased amplitudes of the discharge and ion currents oscillations [14]. Two distinct, linear and nonlinear, response regimes were observed. The rms values of the ion and the discharge currents increased as a result of the externally driven modulations. Effect of the modulation on the thruster efficiency was investigated in terms of the current and propellant utilization coefficients. The total contribution to the thruster efficiency defined as a product of the above two coefficients, shows the increase up to 20%, compared to regimes without the external drive. Similar results trend was shown in recent work by Wei *et al* [40]; however, in their work amplification of the breathing mode was due to changes in thruster operating parameters.

Results of the experiments and our simulations with 1D model suggest that the observed behavior is due to decrease of phase shift between ion velocity and ion density oscillations, increase in the amplitudes for both quantities, as well as the contribution of the average of the nonlinear (quadratic) terms. Combination of these effects leads to the rapid increase of the mean ion current in nonlinear regime.

One has note that the total thruster efficiency is also affected by other factors (electrical utilization efficiency, discharge voltage utilization), so that the total efficiency will be lower than the current and propellant utilization.

In summary, the experiments with the external modulations of applied voltage reveal the nonlinear regime of the response of the breathing mode oscillations. In this regime, controlled amplification of the breathing mode results in the improvement of the thruster performance in terms of the

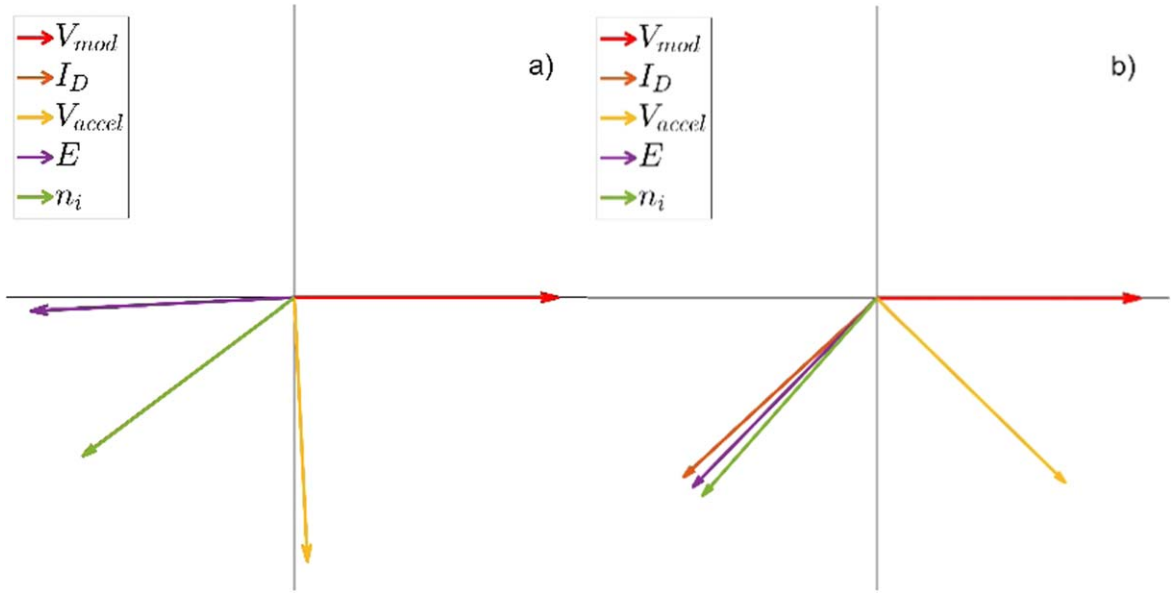

Figure 14. Phasor plots for linear (a) and nonlinear (b) regimes. Modulation voltage was chosen as a reference, and has 0° phase shift. In the nonlinear regime (b) the electric field E phase almost coincides with the ion density n_i and the discharge current I_D, contrary to the linear regime when there is a finite phase difference (of the order of ∼40°) between the electric field and ion density. Note that the discharge current is almost in phase with ion density, both in (a) and (b).

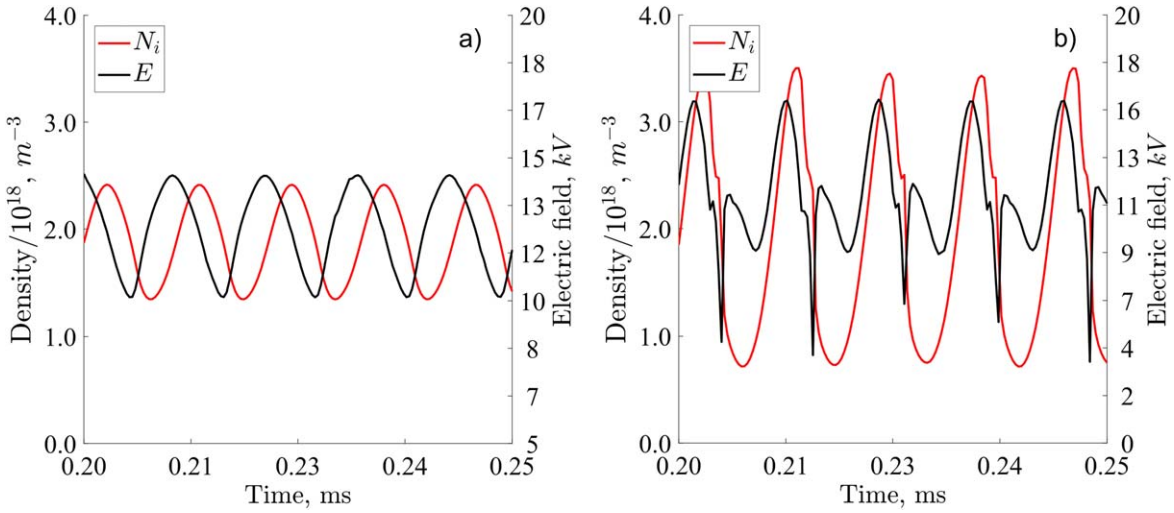

Figure 15. Ion density and the electric field at the exit plane at (a) $V_{\mathrm{mod}} = 0.05U_d$, and (b) $V_{\mathrm{mod}} = 0.5U_d$ modulation amplitude.

current and propellant utilization. These main features, observed experimentally, have been qualitatively reproduced in a simple theoretical model.

Acknowledgments

This work was supported by AFOSR. We acknowledge Yuan Shi, Scott Keller, Ahmed Diallo, Ken Hara, and Igor Kaganovich for fruitful discussions, and Alex Merzhevskiy for his technical support.

Appendix A. Total ion current calculation

The total ion flux and its angular distribution in the plume were measured using a 1.3 cm diameter flat electrostatic probe with the guarding sleeve. The ion collection surface of the probe was at 14 cm from the thruster exit plane. Probe and sleeve were biased relative to the ground to −40 V. The probe current was measured across a 1 kΩ resistor (see figure 2). Probe measurements were taken while probe was rotated between to 0°, ∼20°, and ∼40° relative to the thruster axis. Measurements were conducted during the modulations of the thruster discharge voltage. These results were fitted into the distribution curve, which was taken from previous measurements, which were conducted at similar conditions, but at

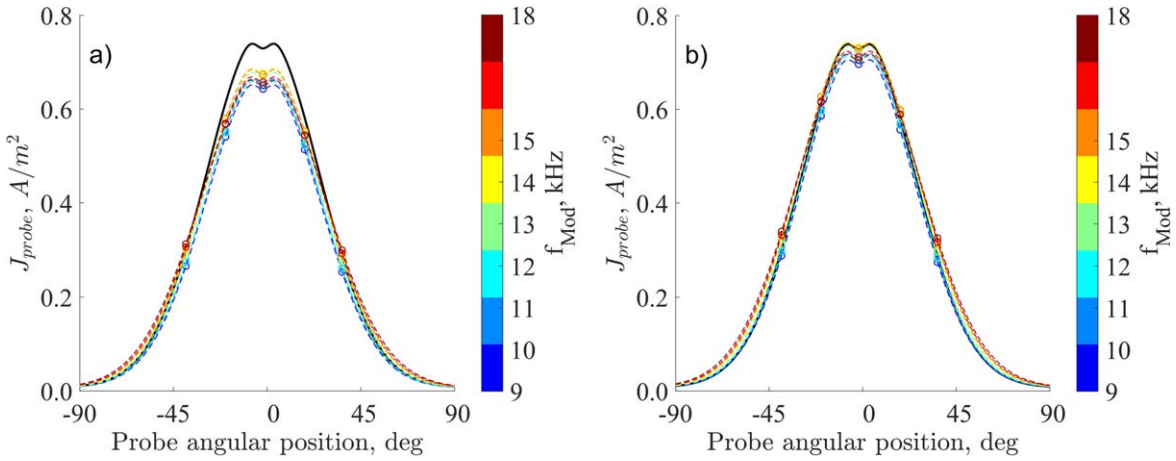

Figure A1. Angular distribution of the ion flux at 10 V modulation amplitude (a), and at 30 V modulation amplitude (b). Different colors represent different driving frequencies. Black line—referenced ion flux distribution at constant discharge voltage.

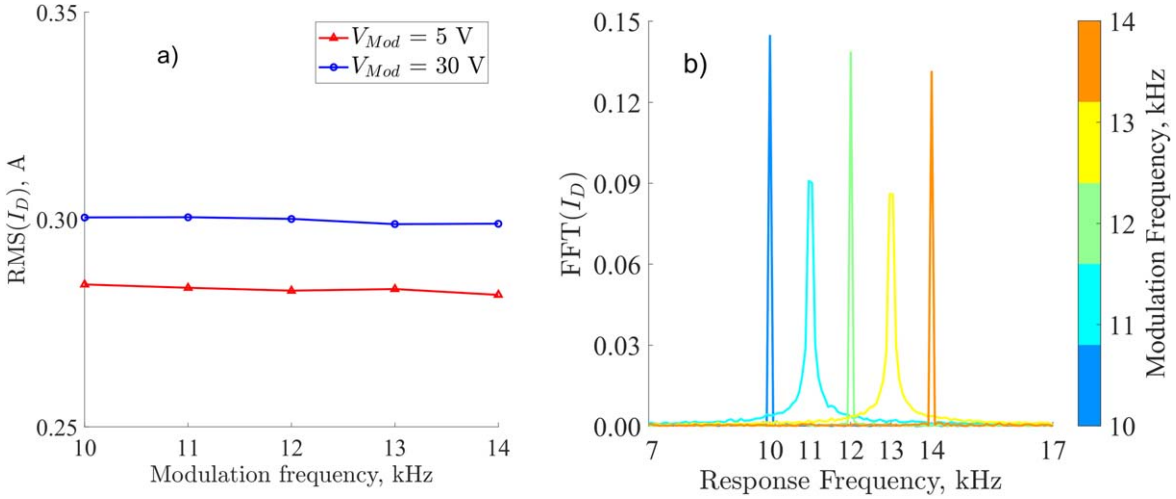

Figure A2. (a) Rms values of the discharge current at different modulation amplitudes; (b) Fourier transforms of the discharge current traces at different modulation frequencies, and 30 V peak-to-peak amplitude. Each color represents different modulation frequency.

constant anode voltage, see [23]. Results for two modulation amplitudes: 10 and 30 V, are shown in figure A1.

The total ion current was estimated by using the following equation

$$J_{\text{ion}} = 2\pi R^2 \int_0^{\pi/2} f \sin\theta \mathrm{d}\theta,$$

where J_{ion} the ion current density.

Appendix B. Effect of the voltage modulations on the circuitry and probe

Because experiments involved modulations of the anode potential with high amplitudes, it was important to verify that there were no parasitic resonances or nonlinear responses from the electric circuit itself. For this purpose, the electrical circuitry was checked for internal resonance frequencies separately from the thruster. The thruster was replaced by 100 Ω 50 W resistor, which was installed between the anode and the cathode power supplies. External modulation with different frequencies and amplitudes was applied, and the discharge current traces were logged. From this data two parameters were determined: rms values of the discharge current and its spectrum. As it is seen from figure A2(a), rms values of the current are uniform over a wide range of frequencies. With the increase of the modulation voltage, current response remains flat. Fourier transforms are shown in figure A2(b). For this case, the modulation voltage amplitude was 30 V peak-to-peak. As one can see there are no additional harmonics. Even though, there is some broadening at 11 and 13 kHz, it did not affect our measurements.

ORCID iDs

I Romadanov https://orcid.org/0000-0003-3291-3341
A Smolyakov https://orcid.org/0000-0002-4975-2743

References

[1] Morozov A 2003 *Plasma Phys. Rep.* **29** 235
[2] Goebel D and Katz I 2008 *Fundamentals of Electric Propulsion: Ion and Hall Thrusters* (New York: Wiley)
[3] Zhurin V, Kaufman H and Robinson R 1999 *Plasma Sources Sci. Technol.* **8** R1–20
[4] Tilinin G 1977 *Sov. Phys. Tech. Phys.* **22** 974
[5] Boeuf J and Garrigues L 1998 *J. Appl. Phys.* **84** 3541–54
[6] Yamamoto N, Komurasaki K and Arakawa Y 2005 *J. Propulsion Power* **21** 870–6
[7] Meezan N and Cappelli M 2002 *Phys. Rev.* E **66** 036401
[8] Bareilles J, Hagelaar G, Garrigues L, Boniface C and Boeuf J P 2004 *Phys. Plasmas* **11** 3035–46
[9] Sankovic J, Hamley J and Haag T 1993 *Proc. 23rd Int. Electric Propulsion Conf. (Seattle)* IEPC93-094
[10] Ito T, Gascon N, Crawford W and Cappelli M 2007 *J. Propulsion Power* **23** 1068
[11] Barral S and Ahedo E 2009 *Phys. Rev.* E **79** 046401
[12] Liqiu W, Chunsheng W, Ke H and Daren Y 2012 *Phys. Plasmas* **19** 012107
[13] Hara K, Sekerak M, Boyd I and Gallimore A 2014 *J. Appl. Phys.* **115** 203304
[14] Romadanov I, Raitses Y, Diallo A, Kaganovich I, Hara K and Smolyakov A 2017 *Proc. 35th Int. Electric Propulsion Conf.*IEPC-2017-267
[15] Raitses Y and Fisch N 2001 *Phys. Plasmas* **8** 2579
[16] Smirnov A, Raitses Y and Fisch N 2002 *J. Appl. Phys.* **92** 5673
[17] Smirnov A, Raitses Y and Fisch N 2003 *J. Appl. Phys.* **94** 852
[18] Smirnov A, Raitses Y and Fisch N 2007 *Phys. Plasmas* **14** 057106
[19] Smirnov A, Raitses Y and Fisch N 2008 *IEEE Trans. Plasma Sci.* **36** 1998
[20] Raitses Y, Smirnov A and Fisch N 2007 *Appl. Phys. Lett.* **90** 221502
[21] Granstedt E, Raitses Y and Fisch N 2008 *J. Appl. Phys.* **104** 103302
[22] Diamant K, Pollard J, Raitses Y and Fisch N 2010 *IEEE Trans. Plasma Sci.* **38** 1052
[23] Raitses Y, Staack D, Dunaevsky A, Dorf L and Fisch N 2003 *Proc. 28th Int. Electric Propulsion Conf.*2003-0139
[24] Romadanov I, Raitses Y, Diallo A, Hara K, Kaganovich I and Smolyakov A 2018 *Phys. Plasmas* **25** 033501
[25] Ahedo E, Martınez-Cerezo P and Martınez-Sanchez M 2001 *Phys. Plasmas* **8** 3058–68
[26] Fruchtman A, Fisch N and Raitses Y 2001 *Phys. Plasmas* **8** 1048–56
[27] Cohen-Zur A, Fruchtman A, Ashkenazy J and Gany A 2002 *Phys. Plasmas* **9** 4363–74
[28] Dorf L, Semenov V and Raitses Y 2003 *Appl. Phys. Lett.* **83** 2551
[29] Smolyakov A, Romadanov I, Chapurin O, Raitses Y, Hagelaar G and Boeuf J 2018 *Phys. Plasmas* in preparation
[30] Dudson B, Umansky M, Xu X, Snyder P and Wilson H 2009 *Comput. Phys. Commun.* **180** 1467–80
[31] Dudson B, Madsen J, Omotani J, Hill P, Easy L and Løiten M 2016 *Phys. Plasmas* **23** 062303
[32] Dudson B, Allen A, Breyiannis G, Brugger E, Buchanan J, Easy L and Xu X 2015 *J. Plasma Phys.* **81** 365810104
[33] Koshkarov O, Smolyakov A, Romadanov I, Chapurin O, Umansky M, Raitses Y and Kaganovich I 2018 *Phys. Plasmas* **25** 011604
[34] Fife J, Martínez-Sánchez M and Szabo J 1997 *33rd AIAA Joint Propulsion Conf.*97-3052
[35] Hara K, Keller S and Raitses Y 2016 *AIAA Propulsion and Energy Forum and Exposition*
[36] Morozov A and Savelyev V 2000 Fundamentals of stationary plasma thruster theory *Reviews of Plasma Physics* vol 21 ed B Kadomtsev and V Shafranov (Boston, MA: Springer) p 201
[37] Barral S, Peradzynski Z, Makowski K and Dudeck M 2001 *High Temp. Mater. Process.: Int. Q. High-Technol. Plasma Process.* **5** 1093-3611
[38] Smirnov A, Raitses Y and Fisch N 2004 *J. Appl. Phys.* **95** 2283
[39] Purves S 2014 *Leading Edge* **33** 1164–6
[40] Wei L, Li W, Ding Y and Yu D 2018 *Plasma Sci. Technol.* **20** 075502